Nanoscale

PAPER

View Article Online
View Journal | View Issue

Cite this: *Nanoscale*, 2023, **15**, 13018

$Ce_{1-x}Zr_xO_2$ nanoparticles in bacterial cellulose, bio-based composites with self-regenerating antioxidant capabilities

Johanna van Gent *[a,b] and Anna Roig *[a]

Received 15th June 2023,
Accepted 18th July 2023

DOI: 10.1039/d3nr02872k

rsc.li/nanoscale

Bacterial cellulose (BC) is an emerging biopolymer with ever-widening uses in the biomedical field due to its purity, mechanical stability, conformability, moisture control, and biocompatibility. In the wet form, its highly porous nanofibrillar structure and abundant surface hydroxyl groups enable the functionalisation of BC with inorganic nanoparticles (NPs), granting the material additional purposive capabilities. As oxidative stress caused by reactive oxygen species (ROS) negatively affects various cellular structures, the functionalisation of BC with CeO_2 NPs, known antioxidants, is pursued in this work to achieve composites capable of minimising inflammation and tissue damage. We report on low-temperature *in situ* syntheses of CeO_2 NPs in BC enabling the formation of BC–CeO_2 composites that exhibit self-regenerating antioxidant properties, as verified by 2,2-diphenyl-1-picrylhydrazyl (DPPH) assays and studies of the evolution in the CeO_2 absorption edge (indicative of the Ce^{3+} and Ce^{4+} fractions). X-Ray photoelectron spectroscopy (XPS) further reveals that incorporation of zirconium into the CeO_2 lattice leads to a four-fold increase in the Ce^{3+}: Ce^{4+} ratio, thereby enhancing the composite antioxidant performance as exemplified by BC–$Ce_{0.6}Zr_{0.4}O_2$ recording the highest %DPPH scavenging per unit mass of NPs among the BC–$Ce_{1-x}Zr_xO_2$ studied systems.

Introduction

Bacterial cellulose (BC) is a type of nanocellulose produced by various Gram-negative bacteria, of which *Komagataeibacter xylinus* (*K. xylinus*) is one of the most prominent.[1,2] Compared to plant-extracted cellulose, BC benefits from the nanoscale features of its fine fibrillar network, high purity, and crystallinity. Its production has a lower environmental footprint while the material presents a larger surface area, high tensile strength, and thermal stability.[3–5] In addition, the soft-hydrogel texture of as-biosynthesised BC makes it an excellent candidate for biomedical applications, where features such as water-retaining capacity, conformability, and tuneability of gas/liquid/ion transport are sought-after characteristics.[3,5–7]

Despite the many structural traits making BC attractive for biomedical uses, the material lacks functional properties. In particular, antioxidant capabilities in BC wound healing patches or internal implants would be desirable since reactive oxygen species (ROS) are well-established culprits for tissue damage in a great variety of ailments and play an important role in the progression of inflammatory disorders.

CeO_2 NPs have been demonstrated to possess unique redox properties suited for various catalytic and sensing applications.[8–11] In addition to CeO_2, $Ce_{1-x}Zr_xO_2$ is also widely employed in environmental catalysis, as a catalyst and as a metal catalyst support, due to its excellent oxygen storage/release capacity,[12,13] high activity and hydrogen selectivity[14] in, for instance, dry-reforming methane reactions.

In the context of biomedical applications, CeO_2 NPs have been studied for their redox enzyme mimetic efficiency and biocompatibility.[15–20] The redox properties of CeO_2 NPs are based on the reversible transition between Ce^{4+} (defectless) and Ce^{3+} (oxygen vacancy) states within its cubic fluorite structure ($Fm\bar{3}m$), both states having significant populations in CeO_2 NPs due to their propensity for oxygen vacancies. The antioxidant properties of CeO_2 NPs in the presence of ROS ($^{\bullet}O^{-}_2$, H_2O_2) occurs through the oxidation of surface Ce^{3+} states, as described by the following equations:

$$Ce^{3+} + {}^{\bullet}O_2{}^{-} + 2H^{+} \rightarrow Ce^{4+} + H_2O_2 \quad (1)$$

$$2Ce^{3+} + H_2O_2 + 2H^{+} \rightarrow 2Ce^{4+} + 2H_2O \quad (2)$$

[a]*Institut de Ciència de Materials de Barcelona (ICMAB-CSIC), Campus UAB, Bellaterra, Spain. E-mail: roig@icmab.es*
[b]*Zernike Institute for Advanced Materials, University of Groningen, Groningen, the Netherlands. E-mail: j.van.gent.gonzalez@rug.nl*

A key feature making CeO_2 NPs particularly attractive as an antioxidant is their ability to regenerate since Ce^{4+} can be reduced back to the Ce^{3+} state:

$$Ce^{4+} + {}^{\bullet}O_2^{-} \rightarrow Ce^{3+} + O_2 \quad (3)$$

$$2Ce^{4+} + 2H_2O_2 \rightarrow 2Ce^{3+} + 2H_2O + 2H^{+} \quad (4)$$

BC has been proposed as a soft material with mechanical and suitable anti-adherent properties capable of overcoming the long-lasting challenge of reducing implant adhesion with internal organs in, for instance, a hernia surgery[21] or after the insertion of cardiac electronic devices.[22] In such scenarios, the functionalisation of BC with CeO_2 NPs can make for an innovative internal implant in which BC is endowed with self-regenerating anti-inflammatory properties.[15,17,18]

Since the antioxidant properties of CeO_2 hinge on the $Ce^{3+} \rightleftharpoons Ce^{4+}$ equilibrium, skewing this towards a larger Ce^{3+} equilibrium population should bolster the antioxidant properties of BC composites. Given the size-dependent facet stability of CeO_2 NPs and, subsequently, the facet-dependent stability of oxygen vacancies, reducing NP size can improve the nanoceria antioxidant properties. Here, a balance should be found between the maximisation of surface area (*i.e.*, area of exposed Ce^{3+}) by decreasing NP size, and minimisation of the energy costs associated with near-surface oxygen vacancy formation by increasing NP size. Thus, suitable synthetic approaches compatible with using BC as a support should be identified.[11,23–26]

This paper aims to add antioxidant (*i.e.*, anti-inflammatory) capabilities to the arsenal of attractive properties making BC suited for wound healing by grafting large surface area ceria (CeO_2) nanoparticles (NPs) to a BC film. To maximise the reducing power of composites (*i.e.*, increase the amount of equilibrium Ce^{3+}), CeO_2–ZrO_2 solid solution NPs are synthesised. Zirconia (ZrO_2) is also a biocompatible metal oxide known to take on its otherwise unstable cubic phase in solid solutions containing >20% CeO_2. Incorporation of ZrO_2 to a cubic CeO_2 lattice is an established strategy for increasing the oxygen storage capability of ceria-based car catalysts[27,28] and has been similarly used to enhance the reducing power of catalytic ceria.[8] This is because ZrO_2 incorporation facilitates the formation of oxygen vacancies in two ways. Firstly, a strained oxygen octahedron forms because Zr^{4+} are smaller than Ce^{3+} cations and much smaller than O^{2-} anions. The formation of an oxygen vacancy relieves the energetic cost associated with this strain. Thus oxygen vacancies take place more readily in CeO_2–ZrO_2 solid solutions when compared to CeO_2. Secondly, the smaller Zr^{4+} cations are better able to accommodate the increase in Ce–O bond length upon Ce^{4+} reduction to Ce^{3+} (driven by oxygen vacancy formation). Therefore, not only is the energy barrier for oxygen vacancy formation lowered, but the resulting oxygen vacancy state is also better stabilised in CeO_2–ZrO_2 solid solutions compared to CeO_2.[13,29]

Experimental

Biosynthesis of bacterial cellulose

K. xylinus bacteria purchased from the Spanish Culture Collection (CECT) are grown in solid Hestrin–Schramm (HS) medium consisting of 2.00% (w/v) D-glucose, 1.50% agar, 0.68% disodium phosphate, 0.50% peptone, 0.50% yeast extract and 0.115% citric acid for 7 days at 30 °C. A colony from the resulting plate is expanded in 6 mL of liquid HS medium using a sterile loop. After incubating at 30 °C for 7 days, 0.50 mL of the resulting liquid bacterial culture is added to 4.5 mL of liquid HS medium and left to incubate at 30 °C for another 7 days. The obtained bacterial culture is mixed with HS medium in a 1 : 15 ratio and is cultured in a well plate at 30 °C for 7 days. Once the BC pellicle forms at the air–liquid interface it is removed and washed using ethanol, Milli-Q water and 0.1 M NaOH. Cleaned BC films are stored in Milli-Q water at ambient temperature.

Synthesis of $Ce_{1-x}Zr_xO_2$ NPs

Solvent exchange from water is performed for wet biosynthesised BC films of rounded shape and diameter (∅) = 1.60 cm by ultrasonicating for 10 min in benzyl alcohol, placing films in a fresh benzyl alcohol solution and subsequently agitating using a variable speed rocker for 4 h.

CeO_2 NPs by oil bath (OB) route. A 20 mL 7.88 mM cerium (III) acetate ($Ce(OAc)_3$) benzyl alcohol solution is ultrasonicated for 15 min before adding four ∅ = 1.60 cm benzyl alcohol-exchanged BC films. The reaction mixture is heated to 185 °C for 4 h, after which the films are washed with ethanol and Milli-Q water (1 : 10) and dried at 70 °C.

CeO_2 NPs by microwave-assisted (MW) route. Microwave-assisted syntheses are performed using a *CEM Discover* microwave synthesizer (2.45 GHz, 300 W). A 4 mL 15.76 mM Ce $(OAc)_3$ solution is ultrasonicated for 15 min and added to a microwave tube with one ∅ = 1.60 cm solvent-exchanged BC film. The reaction mixture is heated in two steps: (i) 5 min at 60 °C and (ii) 30 min at 185 °C, similar to our previous work.[30] The resulting films are washed with ethanol and Milli-Q water (1 : 10) and dried at 70 °C.

$Ce_{1-x}Zr_xO_2$ NPs. To incorporate Zr into CeO_2 the same protocols described above are used, with the addition of an appropriate volume of zirconium(IV) propoxide ($Zr(OPr)_4$) in 1-propanol (70 wt%) to reach the desired Ce : Zr molar ratio. Samples with x = 0.2, 0.4, 0.5 and 0.6 were synthesised. Herein x = 0.4 is discussed as it showed the best performance.

BC composites are labelled as CeO_2 (OB), CeO_2 (MW), $Ce_{0.6}Zr_{0.4}O_2$ (OB) and $Ce_{0.6}Zr_{0.4}O_2$ (MW) respectively. From here on, the first three systems will be discussed further due to the rather low inorganic loading of the $Ce_{0.6}Zr_{0.4}O_2$ (MW) composite.

Material characterisation

Scanning electron microscopy (SEM) imaging and energy dispersive X-ray (EDX) elemental analysis are performed on a *FEI Quanta 200 FEG* scanning electron microscope.

JEOL JEM-1210 electron microscope operating at 120 kV with an ORIUS 831SC600 Gatan camera was used to obtain transmission electron microscopy (TEM) images and diffraction patterns of the nanoparticles using the selected area electron diffraction (SAED) mode. The mean nanoparticle size was determined by measuring the diameter of ~300 NPs on these images.

X-ray diffraction (XRD) measurements are performed on a *Bruker D8 Advance A25* diffractometer to determine the crystalline phase. X-ray photoelectron spectroscopy (XPS) was performed using a hemispherical *SPECS Phoibos 150* analyzer and dual anode X-ray source (Al K_α 1486.7 eV, Ag L_α 2984.3 eV). XPS is a surface-sensitive technique based on the photoelectric effect that measures the kinetic energy of electrons ejected from a given atomic shell upon X-ray irradiation. Since the binding energy depends on the oxidation state, the Ce^{3+}: Ce^{4+} ratio in BC–$Ce_{1-x}Zr_xO_2$ composites is quantified upon fitting the peaks corresponding to the Ce 3d orbitals as the ratio of peak area corresponding to each species.

The antioxidant properties of the composites were verified using a 2,2-diphenyl-1-picrylhydrazyl (DPPH) assay, where 1.5 mL of a 2 mM DPPH solution was pipetted into a well plate containing one ∅ = 1.60 cm BC–$Ce_{1-x}Zr_xO_2$ sample (three samples of each composite type were tested). After gentle (300 rpm) agitation for 8 h, samples were assessed using a *Tecan Infinite 200 Pro* plate reader, where the decrease in intensity of the absorption peak (λ = 520 nm) associated with the *DPPH radical (A) with respect to a blank (A_0) is used to calculate a DPPH scavenging %, indicative of the antioxidant performance of the composites.

A TGA-DSC/DTA analyser (*NETZSCH STA 449 F1 Jupiter*) with a heating rate of 10 °C min^{-1} from room temperature to 800 °C in air was used to evaluate the inorganic NP mass fraction in the nanocomposite films. From these measurements, the DPPH results were normalised by the unit mass of inorganic material.

Diffuse-reflectance UV/vis absorption measurements were performed using a *Jasco V-780* UV/vis spectrophotometer equipped with an integrating sphere to study the time evolution of the cerium oxidation state in BC–$Ce_{0.6}Zr_{0.4}O_2$ composites upon exposure to 1 mM and 5 mM H_2O_2 solutions over two weeks. These tests are performed using H_2O_2 since this is an important reactive oxygen species in many inflammatory scenarios. In addition, the chosen concentrations far surpass the maximum encountered in the human body to ensure the effectiveness of the composites in the most extreme conditions.[31]

Results

We report here the successful synthesis of $Ce_{1-x}Zr_xO_2$ NPs in BC to produce BC composites exhibiting self-regenerating antioxidant properties. The NPs were synthesized *in situ* on wet BC films through low temperature, non-aqueous sol–gel reactions using conventional oil baths and microwave-assisted heating (Scheme 1). Leaching experiments prove that the NPs are well attached to the BC film since no ceria could be detected in the supernatant after one month of immersing BC composites in water. BC–$Ce_{1-x}Zr_xO_2$ composites remain very flexible and foldable, comparable to pristine BC.

SEM and TEM imaging (Fig. 1) and EDX analysis (Table 1) reveal variations in morphology and loading across the various BC–$Ce_{1-x}Zr_xO_2$ composites. BC–CeO_2 composites (OB and MW) present the nanocellulose fibres uniformly decorated with CeO_2 NPs with a mean size of 2.7 ± 0.4 nm but show differences in morphology and loading based on the synthesis mode. OB samples have higher loading and formation of patches of inorganic material at the surface. From TEM electron diffraction (Fig. 1), the lattice parameter of ceria NPs was determined to be 5.48 Å, which aligns with values commonly reported for cubic CeO_2. Furthermore, the brown colour of the OB BC–CeO_2 composite also aligns with previous reports of surface defects (oxygen vacancies) in CeO_2 NPs, resulting in a brown colour.[32,33]

On the other hand, the MW sample is beige, have a slightly smaller lattice parameter, 5.44 Å, and slightly lower NP loading. These features fall in line with previous reports of (relatively) long reaction times and small NP sizes for the microwave-assisted synthesis of CeO_2 NPs,[34,35] where selective heating of polar hydroxyl groups at the BC surface may lead to more favourable nucleation relative to NP growth.

As demonstrated by the % NP mass values obtained by TGA (Table 1), BC–$Ce_{0.60}Zr_{0.40}O_2$ OB samples have significantly less loading than both OB and MW BC–CeO_2. This is corroborated by SEM and TEM imaging, where a thicker superficial coating and smaller number of NPs within the BC matrix are observed.

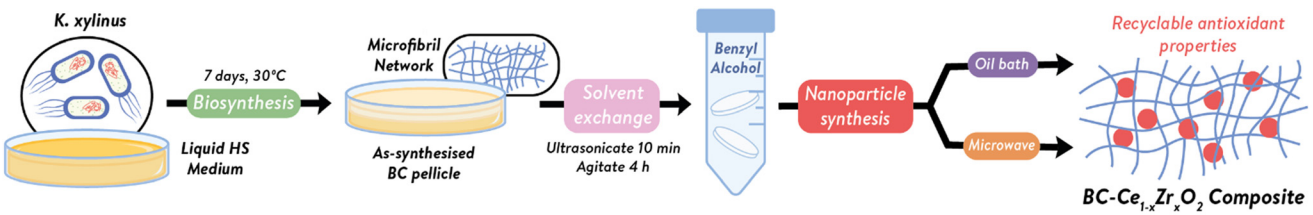

Scheme 1 Schematic overview of the methodology used to prepare bacterial cellulose (BC) composites containing $Ce_{1-x}Zr_xO_2$ nanoparticles.

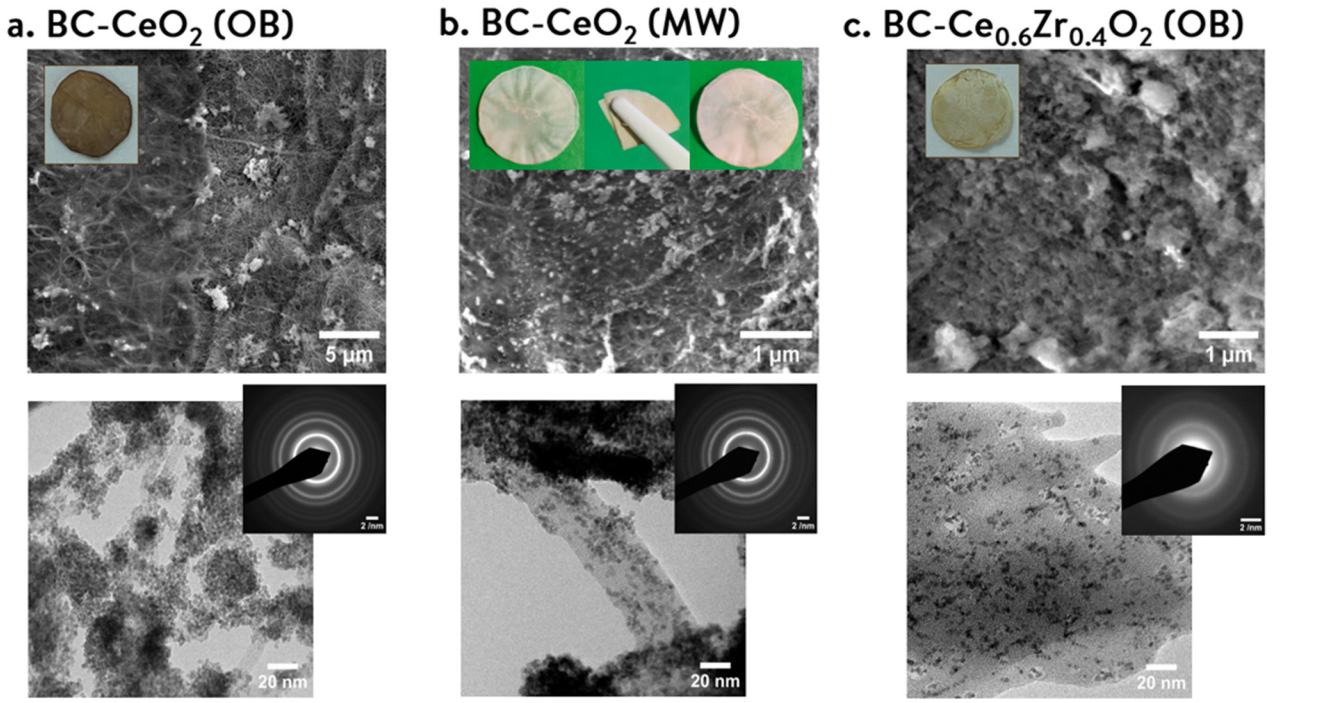

Fig. 1 Upper row, scanning electron microscopy (SEM) images of bacterial cellulose (BC) composite surfaces, insets include a representative film for each condition, inset of (b) shows folding and unfolding of a dried BC–CeO_2, which presents similar mechanical properties than pristine BC. Lower row, transmission electron microscopy (TEM) images of the BC fibers decorated with $Ce_{1-x}Zr_xO_2$ nanoparticles, insets include a selected area electron diffraction (SAED) diffractogram of each system, (a) CeO_2 (OB), (b) CeO_2 (MW), (c) $Ce_{0.6}Zr_{0.4}O_2$ (OB).

Table 1 Results obtained from TEM and TGA. Columns 2 and 3 show the size and lattice parameter of NPs in BC, as obtained by TEM and SAED. Column 4 shows the % inorganic mass in composites, as determined by TGA

NP type	NP size (nm)	a (Å)	TGA % inorganic mass
CeO_2 (OB)	2.7 ± 0.4	5.48 ± 0.01	49
CeO_2 (MW)	2.7 ± 0.4	5.44 ± 0.01	42
$Ce_{0.6}Zr_{0.4}O_2$ (OB)	2.6 ± 0.4	5.37 ± 0.01	14

Based on this distinction it appears that the formation of $Ce_{1-x}Zr_xO_2$ NPs takes place with more difficulty, which may be a consequence of the more strained structure relative to the CeO_2 counterpart. EDX analysis shows a 3 : 2 Ce : Zr ratio, the expected stoichiometry for BC–$Ce_{0.6}Zr_{0.4}O_2$.

X-ray diffraction (Fig. 2) confirms that all systems have a cubic structure and give an indication of the crystalline NP loading within each composite. As the BC–CeO_2 (MW) and BC–$Ce_{0.6}Zr_{0.4}O_2$ (OB) samples does not exhibit a significant intensity of the diffraction peaks compared to BC–CeO_2, it appears that the outer coating observed by SEM/EDX is of amorphous nature.

Comparison of the intensity of CeO_2 XRD peaks between BC–CeO_2 OB and MW samples does not align with observations made by SEM and TGA. While the results of Fig. 2 seem to suggest that NP loading in MW BC–CeO_2 is much lower than those of OB BC–CeO_2, the other measurements show that while NP loading in MW samples is lower than in OB samples, it is not by such a large difference. Furthermore, the sharp diffraction rings from electron diffraction in Fig. 1 imply comparable crystallinity for CeO_2 NPs synthesised through both OB and MW routes. A plausible explanation accounting for such results may be that the CeO_2 NPs in MW samples present a smaller core of crystallinity comparable to OB samples. At the same time, the rest of the NP volume is composed of amorphous material. The smaller lattice parameter yet comparable NP size observed for the MW BC–CeO_2 system can then be accounted for since a smaller crystalline core would impose additional strain forcing CeO_2 to adopt a smaller lattice. Lastly, an amorphous outer shell for MW CeO_2 NPs could explain why MW BC–CeO_2 samples are beige instead of brown since oxygen vacancies at the surface of amorphous cerium oxide will not result in the same absorption characteristics as in crystalline CeO_2. Regarding the origin of the formation of an amorphous shell surrounding a smaller crystalline core, it is possible that the rapid, selective heating at the NP surface under MW irradiation leading to the fast reaction and cooling rates characteristic of the MW synthesis route cause improper crystallisation of the CeO_2 NPs.

From XPS fitting (Fig. 3) the oxidation state of cerium can be compared across the two synthetic routes and materials. Both BC–CeO_2 samples show a majority Ce^{4+} fraction, where

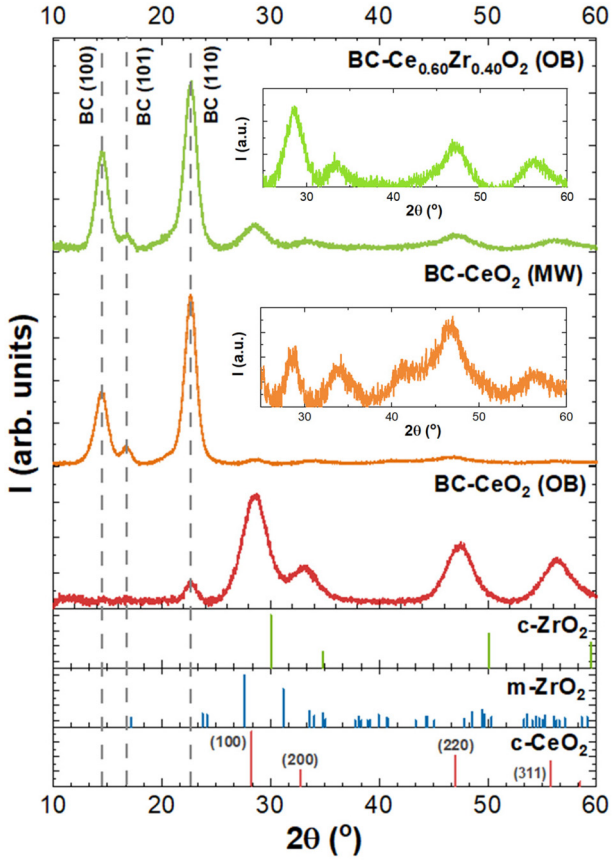

Fig. 2 X-ray diffraction (XRD) diffractograms of BC composites. BC peaks are indicated by grey vertical dashes, while reference monoclinic (m) ZrO_2, cubic (c) ZrO_2 and cubic (c) CeO_2 diffraction patterns are drawn below.

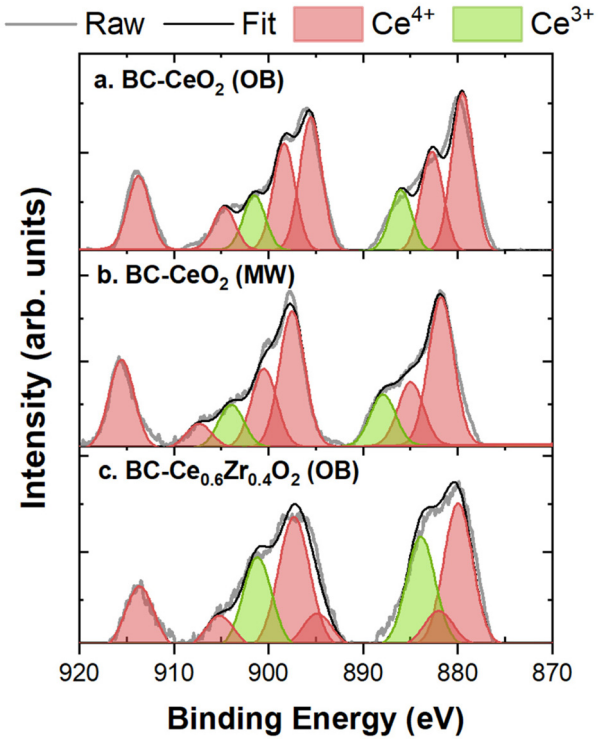

Fig. 3 Fitted X-ray photoelectron spectroscopy (XPS) data of Ce 3d orbitals giving Ce^{3+} and Ce^{4+} equilibrium populations for each BC composite. (a) CeO_2 (OB), (b) CeO_2 (MW), (c) $Ce_{0.6}Zr_{0.4}O_2$ (OB).

the MW sample has a larger equilibrium Ce^{3+} population. This could be due to the greater propensity for oxygen vacancies (*i.e.*, Ce^{3+} formation) in the smaller, more strained CeO_2 crystalline core proposed to be present in MW BC–CeO_2 composites.

Comparison of the cerium oxidation state fractions of BC–CeO_2 with BC–$Ce_{0.6}Zr_{0.4}O_2$ samples reveals a much more prominent difference, with an almost fourfold increase in the Ce^{3+} fraction from the former to the latter. This, along with the significantly ($p < 0.05$) smaller lattice parameter recorded by TEM for BC–$Ce_{0.6}Zr_{0.4}O_2$ when compared to BC–CeO_2 samples (Table 1), confirms both that Zr is successfully incorporated into the cubic CeO_2 structure, and that its addition is an effective way of increasing the equilibrium Ce^{3+} population.

DPPH assay results (Fig. 4) serve to relate the discussed structural features of BC composites to their antioxidant properties. BC–$Ce_{0.6}Zr_{0.4}O_2$ composites outperform OB and MW BC–CeO_2 despite the lower NP loading, demonstrating that there is a positive correlation between the fraction of Ce^{3+} states and the antioxidant performance and that incorporation of Zr into CeO_2 NPs is an effective strategy for enhancing the

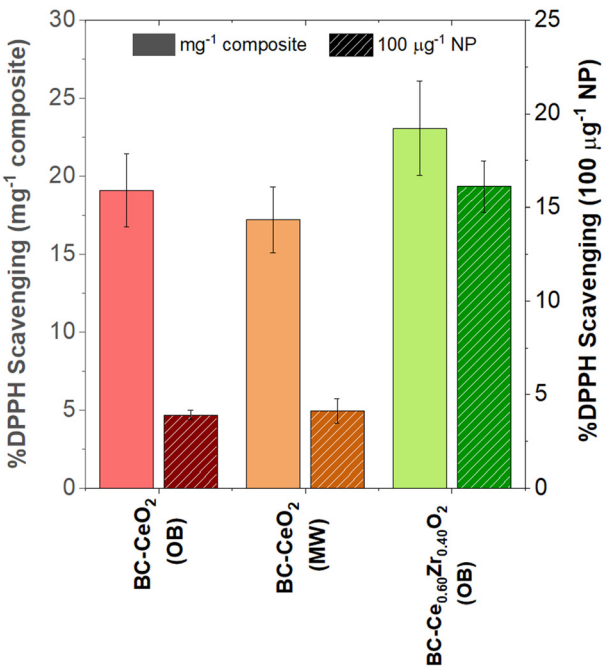

Fig. 4 2,2-Diphenyl-1-picrylhydrazyl (DPPH) assay results for all bacterial cellulose–$Ce_{1-x}Zr_xO_2$ composites showing the %DPPH radical scavenged from a 2 mM DPPH solution over a period of 8 h. The left *y*-axis and solid bars correspond to the %DPPH scavenged per unit mass of the overall composite. The right *y*-axis and dashed bars correspond to the % DPPH scavenged per unit mass of inorganic material.

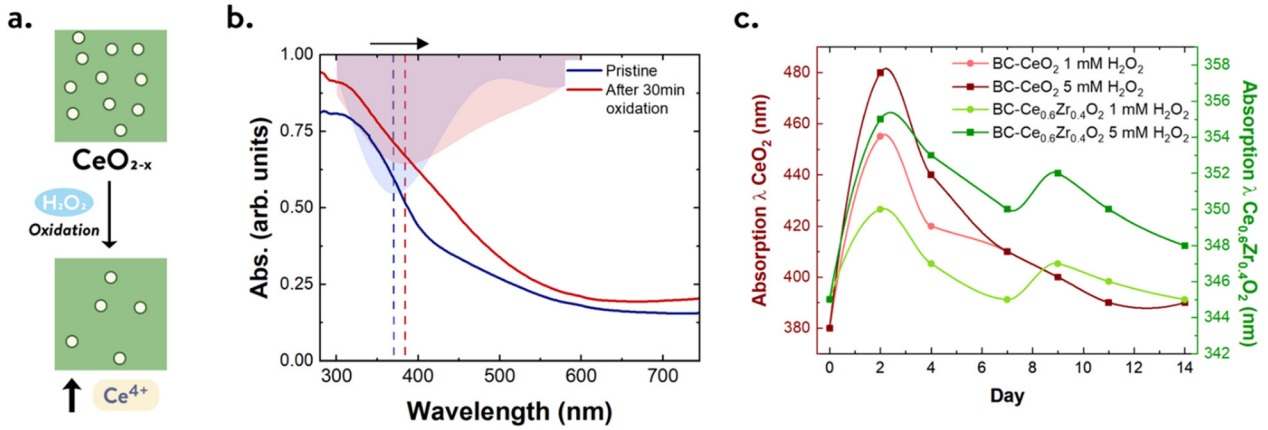

Fig. 5 (a) Schematic diagram of the oxidation process in sub-stoichiometric CeO_{2-x}, in which both the number of oxygen vacancies (white circles) and the Ce^{3+} population decrease. (b) Demonstration of the red-shift in the absorption edge of BC–CeO_2 upon oxidation with 2.12 M H_2O_2 for 30 min (filled translucent blue and red bands correspond to the first derivative of the absorption curves of the corresponding colour). (c) Evolution of the absorption edge wavelength for different BC composites in H_2O_2 solutions over a period of 14 days. The absorption edge is quantified based on the maximum in the derivative of the absorption curve.

antioxidant capabilities of the nanocomposites. Comparison of OB and MW BC–CeO_2 shows similar performances, even though MW BC–CeO_2 shows a slightly higher %DPPH scavenged relative to the amount of NP loading, which may be related to a slightly larger Ce^{3+} fraction shown by XPS (Fig. 3). This demonstrates that it is the number of Ce^{3+} states and not the crystallinity (lower in MW BC–CeO_2) that influence the antioxidant properties of BC–CeO_2 composites.

The self-regeneration of the antioxidant properties in the composites was subsequently tested by diffuse-reflectance UV/vis tracking of the BC composite absorbance over 2 weeks while being immersed in 1 mM and 5 mM solutions of H_2O_2 (Fig. 5). The absorption edge depends on the cerium oxidation state.[36,37] As Ce^{3+} is associated with intrabandgap acceptor states, its conversion to Ce^{4+} leads to a red-shift of the absorption wavelength. This is demonstrated in Fig. 5b, where a BC–CeO_2 film is immersed in 2.12 M H_2O_2 for 30 min, after which the described wavelength shift is observed. Therefore, the wavelength red-shift upon oxidation and the subsequent recovery of the original absorption edge wavelength is indicative of the regenerative nature of BC–CeO_2 samples, which show full recovery within 2 weeks despite the persistent presence of oxidant species in much larger concentrations than those to be expected within the body.[31]

Similarly, the lower wavelength initial absorption edge of BC–$Ce_{0.6}Zr_{0.4}O_2$ samples supports the XPS results, revealing that such samples possess larger equilibrium Ce^{3+} populations.

Compared to BC–CeO_2 films, BC–$Ce_{0.6}Zr_{0.4}O_2$ samples show much smaller wavelength shifts upon oxidation, which also matches observations of BC–$Ce_{0.6}Zr_{0.4}O_2$ composites being less oxidatively damaged when compared to BC–CeO_2 films (BC turns yellow when attacked by H_2O_2). This may be because the quantity of intrabandgap defect states is too large for the decrease in the number of defect states to be noticeable. If one assumes all such intrabandgap states correspond to the oxygen vacancies associated with Ce^{3+} states, the antioxidant capabilities of BC–$Ce_{0.6}Zr_{0.4}O_2$ composites should not be limited by the recovery rate of Ce^{3+} states and would be capable of providing anti-inflammatory relief for extended periods of time.

Conclusions

Bacterial cellulose composites containing $Ce_{1-x}Zr_xO_2$ NPs were successfully synthesised through a low temperature non-aqueous sol–gel reaction using conventional oil baths and microwave-assisted heating on wet BC films. It was demonstrated that the resulting composites possess self-regenerating antioxidant properties whose effectiveness is dependent on the equilibrium populations of Ce^{3+} and Ce^{4+}. Furthermore, adding Zr to CeO_2 NPs increased the Ce^{3+} population, and the BC–$Ce_{0.6}Zr_{0.4}O_2$ composites proved to be the best-performing (4-fold) per unit mass of inorganic loading.

Author contributions

Johanna van Gent: Conceptualization, investigation, visualization, writing – original draft, review & editing. Anna Roig: Conceptualization, methodology, funding acquisition, resources, validation, supervision, writing – review & editing.

Conflicts of interest

There are no conflicts to declare.

Acknowledgements

This work was supported by the Spanish Ministry of Science and Innovation through the PID2021-122645OB-I00 project, the 'Severo Ochoa' Programme for Center of Excellence in R&D (CEX2019-000917), and the Generalitat de Catalunya (2021SGR446 grant). A. R. participate in the Spanish National Research Council (CSIC) interdisciplinary platform for sustainable plastics towards a circular economy (SusPlast), Nanomed Hub CSIC, and the EPNOE network. The authors want to thank Judith Oró, TEM service at ICMAB, for her help with TEM studies.

References

1 A. J. Brown, *J. Chem. Soc., Trans.*, 1886, **49**, 172–187.
2 R. M. Brown, *Food Hydrocolloids*, 1987, **1**, 345–351.
3 D. Klemm, E. D. Cranston, D. Fischer, M. Gama, S. A. Kedzior, D. Kralisch, F. Kramer, T. Kondo, T. Lindström, S. Nietzsche, K. Petzold-Welcke and F. Rauchfuß, *Mater. Today*, 2018, **21**, 720–748.
4 T. Li, C. Chen, A. H. Brozena, J. Y. Zhu, L. Xu, C. Driemeier, J. Dai, O. J. Rojas, A. Isogai, L. Wågberg and L. Hu, *Nature*, 2021, **590**, 47–56.
5 S. M. Choi, K. M. Rao, S. M. Zo, E. J. Shin and S. S. Han, *Polymers*, 2022, **14**, 1080.
6 R. Portela, C. R. Leal, P. L. Almeida and R. G. Sobral, *Microb. Biotechnol.*, 2019, **12**, 586–610.
7 I. Anton-Sales, U. Beekmann, A. Laromaine, A. Roig and D. Kralisch, *Curr. Drug Targets*, 2019, **20**, 808–822.
8 A. Trovarelli, *Catal. Rev.*, 1996, **38**, 439–520.
9 L. Fan, C. Wang, M. Chen and B. Zhu, *J. Power Sources*, 2013, **234**, 154–174.
10 P. Jasinski, T. Suzuki and H. U. Anderson, *Sens. Actuators, B*, 2003, **95**, 73–77.
11 F. Jiang, S. Wang, B. Liu, J. Liu, L. Wang, Y. Xiao, Y. Xu and X. Liu, *ACS Catal.*, 2020, **10**, 11493–11509.
12 Y. Ding, Z. Wang, Y. Guo, Y. Guo, L. Wang and W. Zhan, *Catal. Today*, 2019, **327**, 262–270.
13 Y. Nagai, T. Yamamoto, T. Tanaka, S. Yoshida, T. Nonaka, T. Okamoto, A. Suda and M. Sugiura, *Catal. Today*, 2002, **74**, 225–234.
14 F. Zhang, Z. Liu, X. Chen, N. Rui, L. E. Betancourt, L. Lin, W. Xu, C.-J. Sun, A. M. M. Abeykoon, J. A. Rodriguez, J. Teržan, K. Lorber, P. Djinović and S. D. Senanayake, *ACS Catal.*, 2020, **10**, 3274–3284.
15 Y. Yang, Z. Mao, W. Huang, L. Liu, J. Li, J. Li and Q. Wu, *Sci. Rep.*, 2016, **6**, 35344.
16 M. J. Akhtar, M. Ahamed and H. Alhadlaq, *Molecules*, 2021, **26**, 5416.
17 T. Pirmohamed, J. M. Dowding, S. Singh, B. Wasserman, E. Heckert, A. S. Karakoti, J. E. S. King, S. Seal and W. T. Self, *Chem. Commun.*, 2010, **46**, 2736–2738.
18 C. Korsvik, S. Patil, S. Seal and W. T. Self, *Chem. Commun.*, 2007, 1056, DOI: **10.1039/b615134e**.
19 S. M. Hirst, A. S. Karakoti, R. D. Tyler, N. Sriranganathan, S. Seal and C. M. Reilly, *Small*, 2009, **5**, 2848–2856.
20 L. Zhang, W. Meng, X. Chen, L. Wu, M. Chen, Z. Zhou, Y. Chen, L. Yuan, M. Chen, J. Chen and P. Shui, *ACS Appl. Mater. Interfaces*, 2023, **15**, 10341–10355.
21 I. Anton-Sales, S. Roig-Sanchez, K. Traeger, C. Weis, A. Laromaine, P. Turon and A. Roig, *Biomater. Sci.*, 2021, **9**, 3040–3050.
22 F. Robotti, I. Sterner, S. Bottan, J. M. Monné Rodríguez, G. Pellegrini, T. Schmidt, V. Falk, D. Poulikakos, A. Ferrari and C. Starck, *Biomaterials*, 2020, **229**, 119583.
23 T. Suzuki, I. Kosacki, H. U. Anderson and P. Colomban, *J. Am. Ceram. Soc.*, 2001, **84**, 2007–2014.
24 P. Pérez-Bailac, P. G. Lustemberg and M. V. Ganduglia-Pirovano, *J. Phys.: Condens. Matter*, 2021, **33**, 504003.
25 M. Nolan, S. C. Parker and G. W. Watson, *Surf. Sci.*, 2005, **595**, 223–232.
26 Z.-G. Wang, W.-Z. Bi, S.-C. Ma, N. Lv, J.-L. Zhang, D.-H. Sun and J.-Z. Ni, *Part. Part. Syst. Charact.*, 2015, **32**, 652–660.
27 P. Fornasiero, R. Dimonte, G. R. Rao, J. Kaspar, S. Meriani, A. Trovarelli and M. Graziani, *J. Catal.*, 1995, **151**, 168–177.
28 C. E. Hori, H. Permana, K. Y. S. Ng, A. Brenner, K. More, K. M. Rahmoeller and D. Belton, *Appl. Catal., B*, 1998, **16**, 105–117.
29 M. Alifanti, B. Baps, N. Blangenois, J. Naud, P. Grange and B. Delmon, *Chem. Mater.*, 2003, **15**, 395–403.
30 S. Roig-Sanchez, E. Jungstedt, I. Anton-Sales, D. C. Malaspina, J. Faraudo, L. A. Berglund, A. Laromaine and A. Roig, *Nanoscale Horiz.*, 2019, **4**, 634–641.
31 H. J. Forman, A. Bernardo and K. J. A. Davies, *Arch. Biochem. Biophys.*, 2016, **603**, 48–53.
32 K. R. Singh, V. Nayak, T. Sarkar and R. P. Singh, *RSC Adv.*, 2020, **10**, 27194–27214.
33 Z. Chen, Y. Ding, N. Fang and C. Liu, *Mater. Res. Express*, 2018, **5**, 065905.
34 J. Shi, H. Wang, Y. Liu, X. Ren, H. Sun and B. Lv, *Inorg. Chem. Front.*, 2019, **6**, 1735–1743.
35 A. Garzón-Manjón, A. Aranda-Ramos, B. Melara-Benítez, I. Bensarghin, J. Ros, S. Ricart and C. Nogués, *Bioconjugate Chem.*, 2018, **29**, 2325–2331.
36 J. M. Perez, A. Asati, S. Nath and C. Kaittanis, *Small*, 2008, **4**, 552–556.
37 M. Das, S. Patil, N. Bhargava, J.-F. Kang, L. M. Riedel, S. Seal and J. J. Hickman, *Biomaterials*, 2007, **28**, 1918–1925.